Propagation mechanism of reverse bias induced defects in Cu(In,Ga)Se2 solar cells

Hanna Nilsson Åhman, Teun Burgers, Nicolas Barreau, Arthur Weeber, Mirjam Theelen

To cite this version:

Hanna Nilsson Åhman, Teun Burgers, Nicolas Barreau, Arthur Weeber, Mirjam Theelen. Propagation mechanism of reverse bias induced defects in Cu(In,Ga)Se2 solar cells. Solar Energy Materials and Solar Cells, 2020, 205, pp.110249. 10.1016/j.solmat.2019.110249 . hal-02445285

HAL Id: hal-02445285
https://hal.science/hal-02445285v1

Submitted on 24 Jun 2022

HAL is a multi-disciplinary open access archive for the deposit and dissemination of scientific research documents, whether they are published or not. The documents may come from teaching and research institutions in France or abroad, or from public or private research centers.

L'archive ouverte pluridisciplinaire **HAL**, est destinée au dépôt et à la diffusion de documents scientifiques de niveau recherche, publiés ou non, émanant des établissements d'enseignement et de recherche français ou étrangers, des laboratoires publics ou privés.

Delft University of Technology

Propagation mechanism of reverse bias induced defects in Cu(In,Ga)Se2 solar cells

Bakker, Klaas; Åhman, Hanna Nilsson; Burgers, Teun; Barreau, Nicolas; Weeber, Arthur; Theelen, Mirjam

DOI
10.1016/j.solmat.2019.110249

Publication date
2020

Document Version
Accepted author manuscript

Published in
Solar Energy Materials and Solar Cells

Citation (APA)
Bakker, K., Åhman, H. N., Burgers, T., Barreau, N., Weeber, A., & Theelen, M. (2020). Propagation mechanism of reverse bias induced defects in Cu(In,Ga)Se_2 solar cells. *Solar Energy Materials and Solar Cells*, *205*, [110249]. https://doi.org/10.1016/j.solmat.2019.110249

Important note
To cite this publication, please use the final published version (if applicable).
Please check the document version above.

Copyright
Other than for strictly personal use, it is not permitted to download, forward or distribute the text or part of it, without the consent of the author(s) and/or copyright holder(s), unless the work is under an open content license such as Creative Commons.

Takedown policy
Please contact us and provide details if you believe this document breaches copyrights.
We will remove access to the work immediately and investigate your claim.

This work is downloaded from Delft University of Technology.
For technical reasons the number of authors shown on this cover page is limited to a maximum of 10.

© 2020 Manuscript version made available under CC-BY-NC-ND 4.0 license https://creativecommons.org/licenses/by-nc-nd/4.0/

Propagation mechanism of reverse bias induced defects in Cu(In,Ga)Se$_2$ solar cells

Klaas Bakker[a,b], Hanna Nilsson Åhman[a], Teun Burgers[c], Nicolas Barreau[d], Arthur Weeber[b,c], Mirjam Theelen[a].

[a] ECN part of TNO - Solliance, High Tech Campus 21, 5656 AE Eindhoven, The Netherlands.

[b] Delft University of Technology, PhotoVoltaic Materials and Devices (PVMD), Mekelweg 4, 2628 CD Delft, The Netherlands.

[c] ECN part of TNO - Solar Energy, Westerduinweg 3, 1755 LE Petten The Netherlands.

[d] Institut des Matériaux Jean Rouxel (IMN)-UMR 6502, Université de Nantes, CNRS, 2 rue de la Houssinière, BP 32229, 44322 Nantes Cedex 3, France

Abstract

Partial shading of monolithically interconnected Cu(In,Ga)Se$_2$ (CIGSe) modules can lead to the formation of reverse bias induced defects. These localized defects permanently reduce the output of the PV module. The formation and propagation mechanisms of these defects is studied. Understanding these mechanisms can help to prevent or mitigate damage due to partial shading of CIGSe PV modules. A propagation mechanism is proposed based on both compositional changes found at the edges of the reverse bias induced defects and differences in observed propagation patterns caused by the lateral voltage drop over the TCO layer.

Graphical Abstract

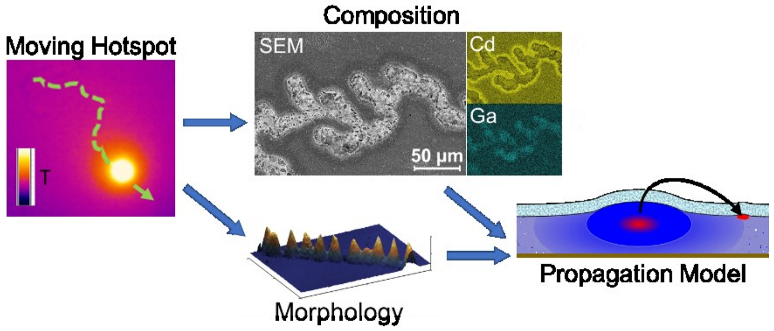

Keywords

Partial shading

Reverse bias

CIGS

Wormlike defects

Propagation mechanism

TCO

1. Introduction

Worldwide installed photovoltaic (PV) capacity is growing and with this growth more PV is installed in urban environments. Application of PV in urban environments has different requirements compared to land based PV farms. Properties like aesthetics for public acceptance and shade tolerance to increase annual output, are more important. Thin-film PV technologies including Cu(In,Ga)Se_2 (CIGSe) have potential advantages to these requirements compared to the mainstream wafer-based crystalline silicon (c-Si) PV modules that are currently dominating the market.

The typical CIGSe PV module is of the monolithically interconnected type. These modules have a unique layout of strings of series connected, long and narrow cells. Major advantage of this design is that CIGSe PV modules are, in general, much more shade tolerant with respect to power loss than c-Si modules [1]. However, the disadvantage of a monolithically interconnected PV module that it is nearly impossible to integrate bypass diodes to protect the individual cells from reverse bias exposure [2].

Reverse bias occurs when one or multiple cells in a module are shaded. The shaded cell is, due to the electrical series connection, forced to conduct more current than it is generating. Due to this imbalance in currents the shaded cell will dissipate power and the operating will point shift toward a negative voltage. This operating condition is often called reverse bias.

Reverse bias in CIGSe modules can lead to local defects, sometimes referred to as “wormlike” defects [3], because of their very distinct visual appearance. Reverse bias induced defects act as local shunts, permanently reducing the module output. These defects originate in local weak spots [4–7] and can be formed relatively easy when no mitigation measures are in place. For example by shades cast from humans or tools [8,9]. Propagation of defects as observed with thermal imaging [3,5] occurs in the form of a moving hotspot. This hotspot leaves a trail that consists of individual islands [3] of a porous material that are argued to start at the interface with the buffer layer [2]. However, up to now there is no real understanding of the mechanism behind the formation and propagation of these defects.

In this work a propagation mechanism is proposed that explains the formation and propagation of the reverse bias induced defects. This mechanism is based on extensive studies of propagation patterns and the composition of wormlike defects. The results of this study can be used to prevent or mitigate damage induced by partial shading of CIGSe PV modules in the future.

2. Materials and methods

2.1. Samples used

The layer stack of the CIGSe solar cells used in this study consists of: 1 mm soda-lime glass (SLG), 500 nm DC-sputtered molybdenum (Mo), 2 µm co-evaporated CIGSe, 50 nm chemical bath deposited cadmium sulfide (CdS), 65 nm DC sputtered intrinsic zinc oxide (i-ZnO), 1 or 2 µm DC sputtered aluminum doped zinc oxide (Al:ZnO) as transparent conductive oxide (TCO) and 60 nm thermally evaporated gold (Au) contacts. The cell layout used closely resembles a cell in a monolithically interconnected commercial module, including analogues for P1 and P3 scribes. The P1 equivalent was created by electrochemically etching part of the molybdenum back contact prior to CIGS deposition. Before gold deposition the P3 equivalent was made by scratching away the full layer stack from the molybdenum with a blade. The cell area is approximately 5 x 7 mm^2 and the cells are without grid, therefore the efficiency is lower compared to cells with metal contacts and very thin TCO. A schematic of the cell design is given in Figure 1. More information on the cell design and manufacturing proces can be found in previous work [10,11] and a description of the 3-stage CIGSe co-evaporation process is given by Couzinie-Devy et al. [12].

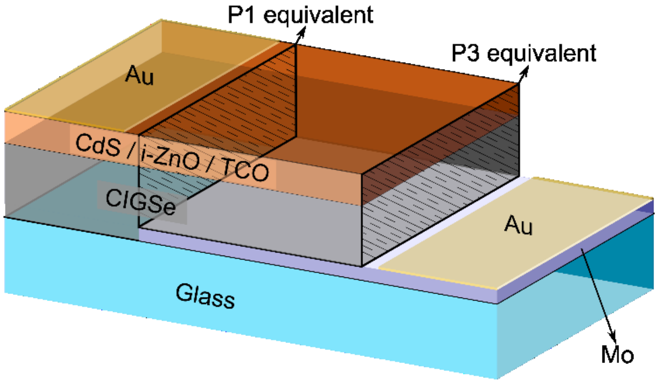

Figure 1: Schematic representation of the cell layout (not to scale). Active cell area is approximately 5 x 7 mm^2, current collection from the Mo and TCO is done at the gold contacts. Hatched cross sections represent the P1 and P3 analogues as found in commercial monolithically interconnected modules.

For this study ten samples from three different CIGSe deposition runs were used. The variations between runs were:

- Run I: 6 samples, standard processing and used as reference.
- Run II: 2 samples, slightly higher Cu flux during 2nd stage of the 3-stage CIGSe co-evaporation deposition resulting in a different Ga profile.
- Run III: 2 samples, substrates with Na barrier and the same CIGSe deposition conditions as run II. Additionally a Na post-deposition treatment (PDT) [13] was carried out.

To study the influence of the TCO on reverse bias behavior of the cells both the TCO layer thickness and deposition tools were varied. The sputter tools used for deposition are located at the Institut des Matériaux Jean Rouxel of the Université de Nantes in Nantes, France and at the Solliance facilities in

Eindhoven, the Netherlands. These sputter tools will be refered to as “Nantes” and “Sollliance”, respectively. On half of the samples from run I a 1 µm thick TCO layer was deposited with the Solliance tool, while on the other half a 2 µm thick layer was deposited using the Nantes tool. On all samples from CIGSe runs II and III the standard 1 µm thick TCO was deposited using the Nantes tool. An overview of the manufacturing parameters for all samples is presented in . The sample name starts either with the run number or with a T for samples with a 2 µm thick TCO.

After reverse bias exposure the layers on top of the CIGSe absorber of samples I-3 and T-2 were removed in two stages to allow further analyses. In the first stage a 1 wt.% acetic acid (HAc) solution was used to remove the TCO by dipping for 3 and 6 minutes for the sample with 1 and 2 µm thick TCO, respectively. The samples were subsequently etched using a 3 wt.% hydrochloric acid (HCl) solution for 15 minutes to completely remove the remaining ZnO and CdS [14].

Table 1: The most important process and sample parameters, the efficiency before and after reverse bias (RB), and information on defect formation. The values for current density (J_{t1}) and voltage (V_{t1}) just before electrical breakdown are presented as well.

Sample name	CIGSe run	CIGSe variation	TCO sputter tool	thickness TCO (µm)	Initial η (%)	after RB η (%)	J_{t1} (mA/cm^2)	V_{t1} (V)	Defects
I-1	Run I	Standard	Solliance	1	11.9	0.0	7.5	6.5	Mobile
I-2	Run I	Standard	Solliance	1	12.4	12.6	-	-	None
I-3	Run I	Standard	Solliance	1	12.4	0.0	6.2	8.2	Mobile
T-1	Run I	Standard	Nantes	2	11.6	1.5	7.8	7.8	Stationary
T-2	Run I	Standard	Nantes	2	12.5	1.4	27.7	8.8	Stationary
T-3	Run I	Standard	Nantes	2	12.1	0.0	211.2	9.4	Stationary
II-1	Run II	Cu flux	Nantes	1	11.4	0.0	12.1	7.1	Mobile
II-2	Run II	Cu flux	Nantes	1	12.9	0.0	1.0	9.1	Mobile
III-1	Run III	Na PDT*	Nantes	1	15.0	13.5	6.9	7.0	None visible
III-2	Run III	Na PDT*	Nantes	1	14.3	0.0	1.2	7.0	Mobile

* PDT: Post-deposition treatment.

2.2. Reverse bias exposure

Wormlike defects as observed in commercial CIGS solar modules were replicated on small solar cells by exposing them to a controlled voltage sweep in the reverse direction. The voltage sweep was executed by a Keithley 2400 source measure unit (SMU), controlled by a computer using the RERA Tracer 3 software. The sweep settings used are: start voltage +0.7 V; end voltage -10.0 V; step voltage 50 mV; scan speed 100 mV/s; current limit 100 mA. The reverse bias (RB) sweeps were carried out in the dark. The current limit of 100 mA was selected because it is the current generated in approximately 3 cm^2 of a neighboring cell that is fully illuminated. Furthermore, this value is in the range of currents (30 – 100 mA) observed during the formation of wormlike by Guthrey et al. [6].

2.3. Characterization

Solar cell parameters were recorded with current density – voltage (*JV*) measurements both under AM 1.5 illumination and in the darkn using a Neonsee class AAA solar simulator. This system was calibrated with a Konica Minolta AK200 reference cell. Scanning electron microscopy (SEM) including elemental analyses with energy-dispersive X-ray spectroscopy (EDX) were performed using a JEOL JSM-6010LA IntouchScope. Raman spectroscopy was executed using a Renishaw inVia Raman microscope with a 632 nm HeNe (Red) and a 514 nm Ar ion (green) laser. For optical and confocal microscopy a Leica MZ12.5 and a Leica DCM 3D were used, respectively. To generate the SEM-EDX image of Figure 6 an acceleration voltage of 10 keV was used. For the elemental maps the L, L, K, and K lines were used for Cd, In, Ga and Cu, respectively. The cross section of Figure 10 (a) was made by

Eurofins material science using a focused ion beam (FIB) and a FEI Nova 200 NanoLab system. Lock-in thermography was done on a system from Infratec that uses IR LEDs as excitation source.

3. Experimental results

3.1. Reverse bias results

Figure 2 shows the *JV* results of a reverse bias sweep for cells with (red) and without defect formation. The formation of a defect (between t1 and t2 in Figure 2) is a very fast process. It occurs during the acquisition of 1 datapoint (500 ms) and is characterized by a sharp increase in current. It is likely for the defects to be formed even faster, as Wendlandt et al. [15] reported the formation of wormlike defects in modules within one 10 ms *JV* measurement. During the propagation phase (between t2 and t3), the measurement system is operating at a fixed current limit and the voltage is fluctuating. The propagation voltage is the average voltage during the propagation phase, and is an indication of the voltage needed for propagation. This voltage provides information on the electric field inside the defect during propagation.

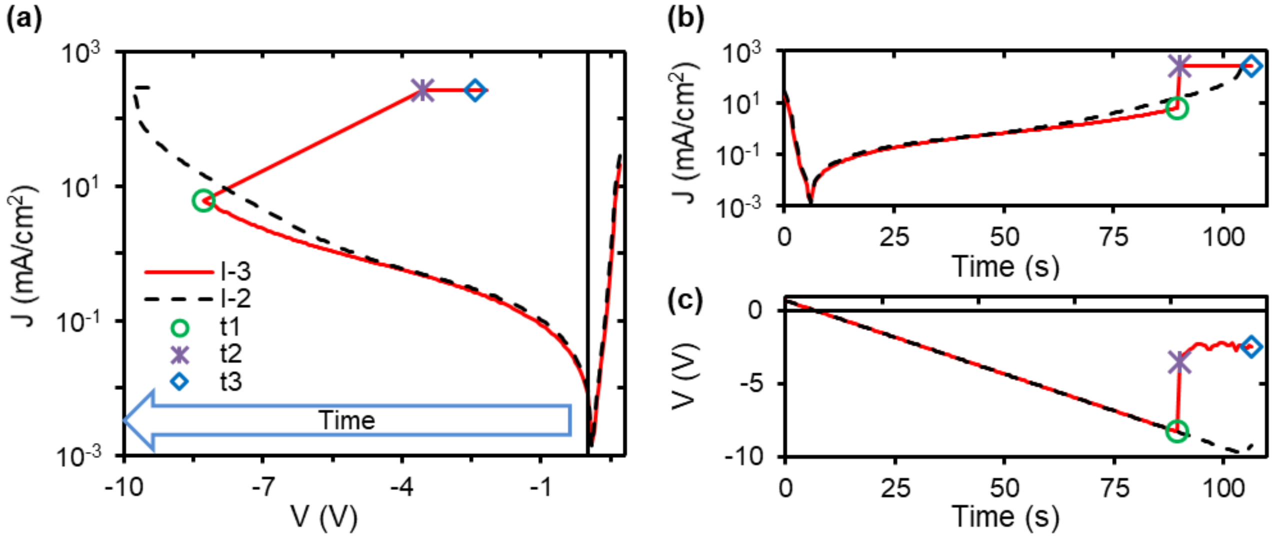

Figure 2: Results of the reverse bias treatment for samples I-3 (red line) and I-2 (black dashed line) with and withouth visible wormlike defect formation, respectively. The individual graphs display (a) the current density (*J*) as function of voltage (*V*), (b) *J* versus time and (c) *V* as function of time. Points of interest are marked. The starting point of the formation of the defect is point t1 (green circle), the first point after defect formation at current limit is point t2 (purple asterisk) and point t3 is the end of the sweep (blue diamond).

The propagation voltage of all cells with visible wormlike defects is plotted in Figure 3. Samples with a thick TCO have a smaller propagation voltage compared to samples with a thin TCO. This implies that the propagation voltage is influenced by the TCO thickness and the associated change in lateral conduction of the TCO with layer thickness. Next to the TCO thickness, the CIGSe absorber material properties also has an effect.

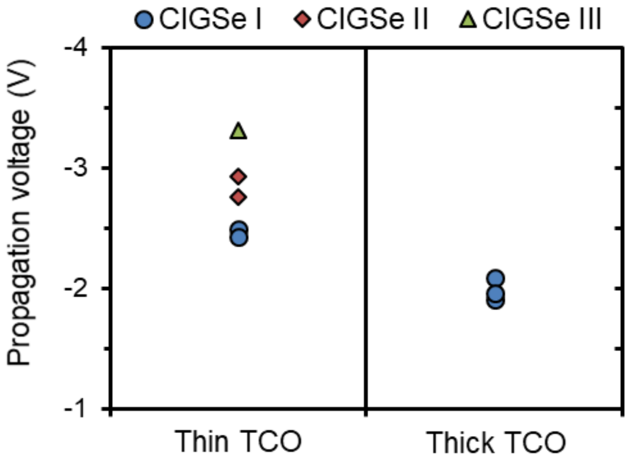

Figure 3: Voltage during propagation phase (average voltage between t2 and t3 in Figure 2 (c)) of all samples that showed visible wormlike defects. On the left samples with 1 µm TCO thickness and on the right samples with 2 µm thick TCO are shown. The blue circles, red diamonds and green triangles represent run I, run II and run III, respectively.

The solar cell efficiencies before and after reverse bias exposure are listed in . Two samples still have efficiencies above 10 % after the RB exposure and do not show visible wormlike defects, which is in contrast to the eight severely degraded cells that all showed visible defects. The current density (J_{t1}) and voltage (V_{t1}) just before the defect formation (t1 in Figure 2) are also listed in . The voltages at which the defects start to form are in the range of 6.5 to 9.4 V. The upper limit of this range is close to the limit of the *JV* sweep (10 V). Therefore, the voltage needed to get a defect started for the surviving cell (I-2) is more than 10 V. The other cell (III-1) that did not exhibit a wormlike defect did lose some efficiency because a small shunt was formed at the edge of the cell after the reverse bias sweep. The current densities at which defects start to form are in general much lower than J_{sc}. This is in agreement with the results of Westin et al. [3] who created wormlike defects by injecting a current equivalent to the short circuit current.

3.2. Optical microscopy

The visible defects show two distinctly different propagation patterns, which are classified as "mobile" and "stationary" wormlike defects. The visual observations after classification, for all cells, are included in and pictures of representative examples of the two classes can be found in the cropped microscope images in Figure 4.

The stationary wormlike defects were found exclusively on the cells with thick TCO, and are not completely detrimental to the cell as long as they did not extend to the P1 analogue. Mobile defects were found on samples with thin TCO. All mobile defects extended to the P1 analogue, resulting in completely shunted cells. Furthermore, the mobile defects propagated along the P1 analogue as was also observed by Lee et al. [2] and Westin et al. [3]. The defects did not cross the P1 analogue into the region without molybdenum underneath the absorber, which means that the defects are only created in areas where an electric field is present between the molybdenum back and the TCO front contact.

The defect in Figure 4 (a) seems to have originated at the border where the CIGS was mechanically removed (P3 analogue) at the right side of the picture. Several studies [4–7] showed that wormlike defects originate at local weak spots. A mechanically defined edge could be a local weak spot; though, only 3 out of 8 wormlike defects started at a mechanically defined edge.

Lock-in thermography has been performed on the samples before and after reverse bias exposure. The thermal pattern shows that the traces of the wormlike defects are locally heated and thus locally shunted. However, no quantitative information can be obtained from these measurements.

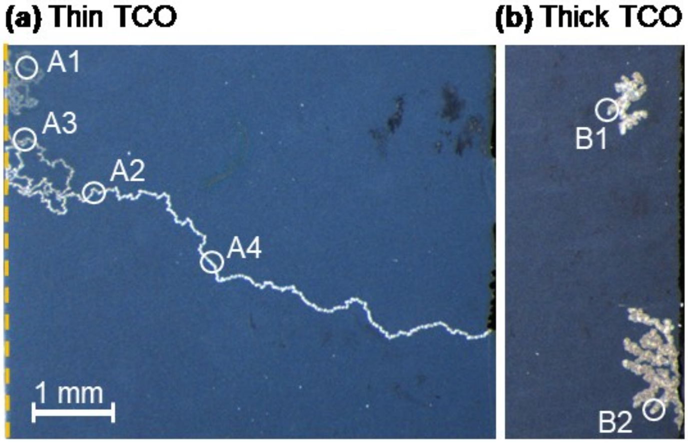

Figure 4: Cropped microscope pictures of two cells with wormlike defects that show different propagation patterns. (a) Sample I-3 with “mobile” wormlike defects and a thin TCO. (b) Sample T-2 with “stationary” wormlike defects and a thick TCO. The numbered circles (A1-A4 and B1+B2) are indications of the positions used for different analyses in the rest of this article. The orange dashed line on the left in (a) indicates the border between areas with and without wormlike defects, this line coincides with the area where the molybdenum stops underneath the absorber, and is analogue to the P1 scribe in a monolithically interconnected module. This line is not shown in (b) because it is located far away from the stationary wormlike defects and outside of the cropped area.

3.3. Confocal microscopy

Confocal microscopy revealed that wormlike defects consist of a chain of protruting “islands”, often higher than a micrometer above the original surface. Figure 5 shows confocal microscope images of samples with two different TCO thicknesses. The stationary wormlike defects (thick TCO) consists of much larger islands compared to the mobile wormlike defects. This trend was observed on all samples. In order to quantify the size of the trails, the islands size is measured at the base of the islands and the spacing between peaks of two islands is measured for a number of different spots.

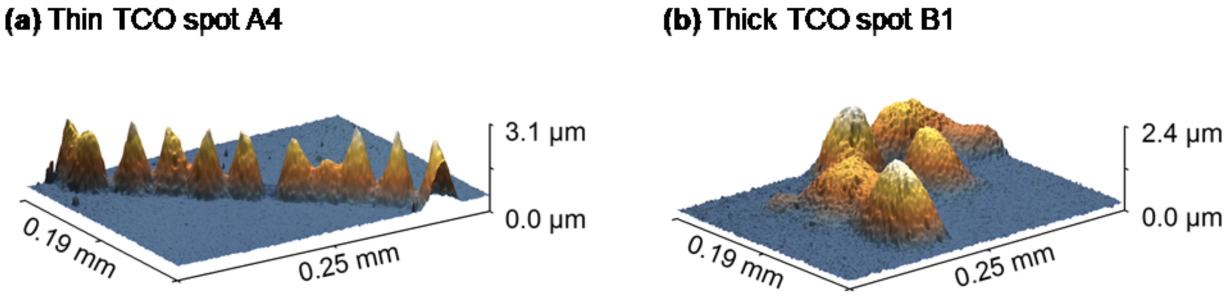

Figure 5: Confocal microscope pictures of wormlike defects on positions A4 and B1 indicated in Figure 4. (a) Spot A4 on sample I-3 with mobile wormlike defects and thin TCO. (b) Spot B1 is on sample T-2 with thick TCO and stationary wormlike defects.

The average sizes and distances between individual islands as well as the height of the islands are listed in Table 2. On sample I-3 there is a large variation between the different spots. Measurements show that the size of the islands in the beginning of the mobile worm (spot A4) is larger than islands formed at a later stage (spot A1 and A3). A possible explanation for the difference in island size is that trails that have already been formed consume part of the total supplied energy. Therefore less energy is available for the growth of the newer individual islands during the formation of a new trail. The stationary wormlike defects of sample T-2 are, compared to samples with thin TCO, much wider and spaced further apart. This is an indication for a difference in island formation and propagation between the samples with different TCO thicknesses.

Table 2: List of average island parameters obtained with confocal microscopy on the positions indicated with colored circles in Figure 4.

Sample and Position	Height (µm)	Width (µm)	Distance (µm)
I-3 A1	0.4 ± 0.1	19 ± 5	18 ± 5
I-3 A2	1.5 ± 0.1	27 ± 3	28 ± 6
I-3 A3	1.0 ± 0.3	19 ± 2	19 ± 4
I-3 A4	2.2 ± 0.3	31 ± 3	27 ± 5
T-2 B1	1.7 ± 0.4	66 ± 15	61 ± 7
T-2 B2	1.5 ± 0.2	70 ± 5	63 ± 4

3.4. SEM analyses

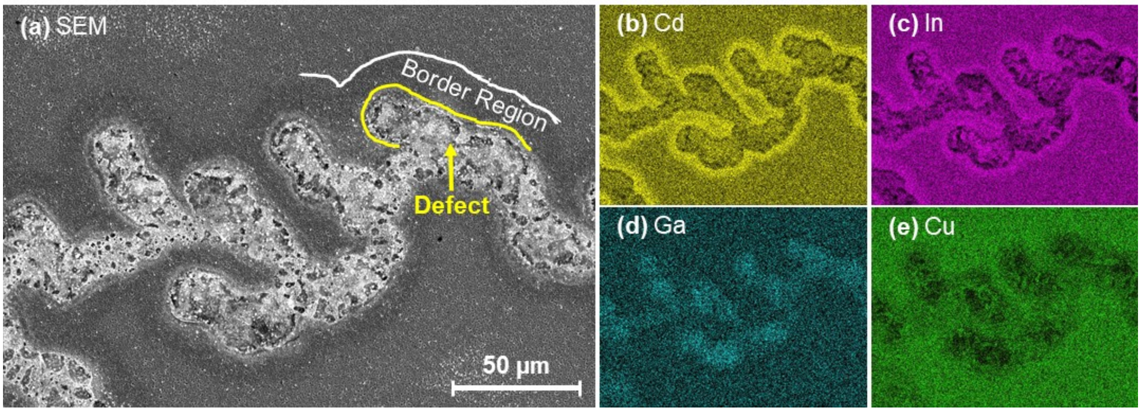

Figure 6 SEM-EDX images of a wormlike defect after HCl etching on sample with thin TCO on spot A3 in Figure 4. (a) SEM image. EDX images of elements (b) Cd, (c) In, (d) Ga and (e) Cu.

SEM-EDX measurements were carried out to study the morphology and composition of the defects. Figure 6 (a) shows a SEM picture of a wormlike defect after removal of the CdS, i-ZnO and Al:ZnO layers on top of the CIGSe. The defect itself consists of a very porous expanded material. This material appears to be molten and re-solidified during formation. The defect has a very distinct border and the material in the border region appears slightly darker in the SEM image. Finally, the unaffected bulk of the CIGSe material further away from the defect, this is used for comparison.

Compositional changes were identified with the aid of EDX. Elemental maps can be found in Figure 6 (b) to (e). The elemental maps are an indication of the presence of the elements and can not be considered in a quantitative way. It should be noted that the peak at 3.29 eV assigned to indium in the EDX analysis also contains a contribution of a secondary cadmium signal. Therefore, the indium signal in Figure 6 (c) is enhanced by the presence of cadmium. More details on quantitative analyses of the elements in the border region can be found in reference [14].The defect shows large areas with lower copper content. Since SEM is a surface technique, it is possible that the copper has migrated towards the back contact. This would agree with the findings of Westin et al. [3] who found higher copper concentrations at the bottom of defects in cross sections of similar defects. Furthermore, a higher gallium concentration is present in the wormlike defect and the indium seems locally depleted in the defect itself.

Furthermore, cadmium and sulfur (not shown) have piled up in the border region. The presence of these elements is surprising as the cadmium sulfide should have been etched away by the HCl. Some possible explanations are:

- The CdS could have reacted to form a compound that is more resilient to the HCl etch.
- The CdS could have diffused into the CIGSe material where it is more difficult to be etched

The pile-up of cadmium combined with the observed changes in composition show that the material in the border region was altered during formation of the defect. In order to study these changes in more detail Raman spectroscopy was performed on the border regions of several defects.

3.5. Raman spectroscopy

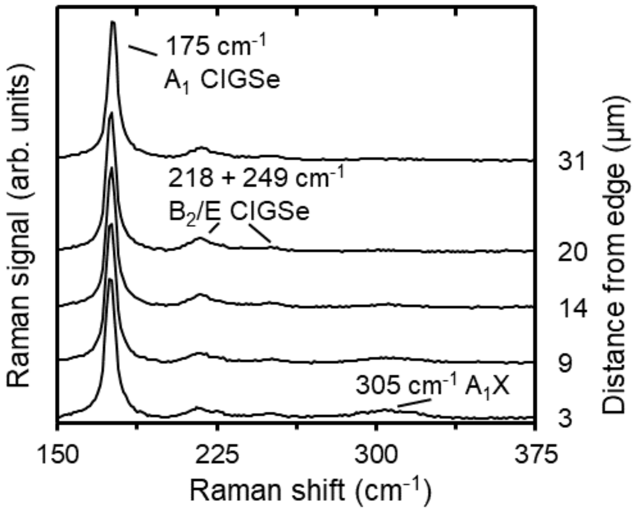

Figure 7: Normalized red laser Raman spectra after baseline correction. On the right axis the progressing distance from the edge of defect at spot A4 in Figure 4 (a) is displayed.

Raman is a nondestructive technique that probes an area of approximately 1-2 µm in diameter with a laser. The material inside the wormlike defect changed to an extent that non-chalcopyrite Raman signals are introduced. These additional signals are non-uniformly distributed over the wormlike defects and often combined into an incoherent mixture of all kinds of phases. However, Raman measurements in the border regions outside the defect give insight in compositional and structural changes that can be related to the propagation mechanism. In Figure 7 the results of a Raman line-scan are plotted. Raman signals away from the defect (top spectrum) are comparable with “as-deposited” (not shown) measurements taken before reverse bias exposure and show a typical Cu(In,Ga)Se$_2$ (CIGSe) fingerprint. Features that are found in this CIGSe spectrum include a dominant peak around 175 cm^{-1}, two smaller peaks around 218 and 249 $cm^{-1,}$ and a very small feature at 305 cm^{-1}. These peaks are commonly assigned to:

- CIGSe A_1 mode around 175 cm^{-1} where its position has a linear relation with the gallium content of the absorber [16].
- Mixed B_2/E acoustical vibration modes in CIGSe [16], for these samples around 218 and 249 cm^{-1}.
- The peak around 305 cm^{-1} is associated either with the A_1 mode of Cu(In,Ga)S_2 (CIGS) [17] or the A_1 mode of CdS [18] and will therefore be referred to as the A_1X peak.

The most obvious change in the spectra of Figure 7 is the emerging A_1X peak when approaching the defect. This peak is still present but hardly distinguishable far away from the defect. Other changes, besides the A_1X peak, were observed in the Raman spectra in the border regions. These changes are not directly visible in the spectra of Figure 7, therefore Raman parameters as function of distance from the edge of the defect are plotted in Figure 8. In this figure, four datasets are combined because the observed trends becomes more pronounced with additional data points. These trends are, to a lesser degree, also present in the samples with thick TCO. The black dashed line in all graphs of Figure 8 represents the as-deposited value, all three parameters start deviating from this line at a distance between 10 to 20 micrometer.

Figure 8 (a) displays the position of the main CIGSe A_1 peak versus the distance to the edge of the defect. In this graph it is observed that the peak position shifts towards lower wavenumbers for points closer to the edge. A shift in the CIGSe A_1 peak position can be attributed to strain in the lattice [16] or changes in gallium [16,19] and copper [19] concentrations. Besides the position also the full width at half maximum (FWHM) of the CIGSe A_1 peak is changing. (Figure 8 (b)). Broadening of the A_1 peak is observed in the vicinity of the defect edge and can be caused by an increased amount of lattice-defects or reduced crystallinity [19].

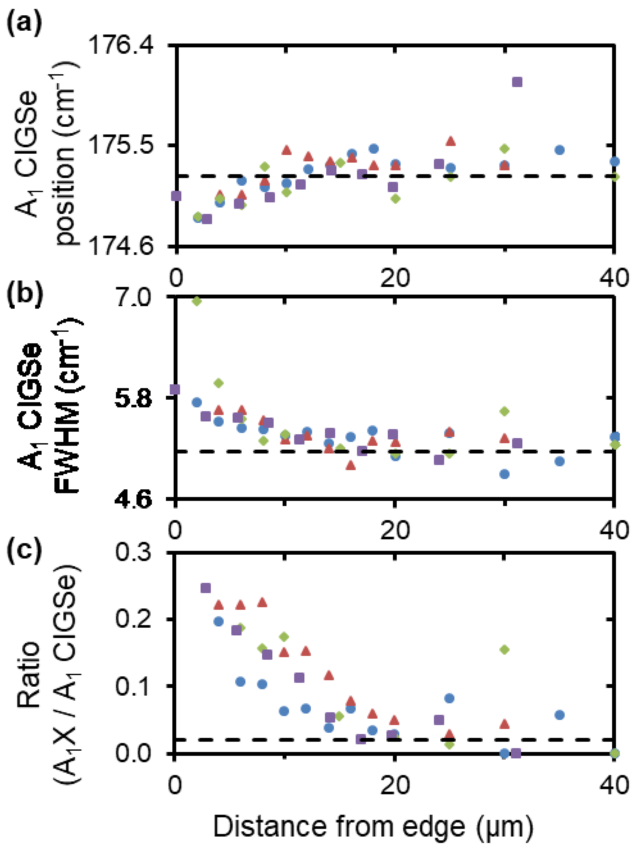

Figure 8: Raman parameters plotted versus distance to the edge of the defect, with on the y axis: (a) A_1 CIGSe peak position, (b) A_1 CIGSe FWHM and (c) A_1X to A_1 CIGSe area ratio. For all graphs the as-deposited values are represented by a horizontal black dashed line. Four datasets have been measured on sample (I-3) with thin TCO, the positions are indicated in Figure 4 (a). Each data set has a different color and symbol.

In order to visualize the increasing magnitude of the A_1X peak, the ratio of the area of the A_1X peak to the main A_1 CIGSe peak is plotted with respect to the distance of the edge of the defect in Figure 8 (c). It is clear that the contribution of the A_1X peak shows a strong increase, starting around 20 µm from the edge, towards the edge of the defect.

One possible explanation for the emerging A_1X peak is the presence of CdS. Oliva et al. [18] stated that a green laser can be used to quantify CdS layer thickness by studying the peak at 600 cm^{-1}. In order to investigate if the A_1X peak originates from the CdS additional Raman measurements with green laser excitation were performed, both before and after the solar cells were etched with HCl to remove the CdS and overlaying layers.

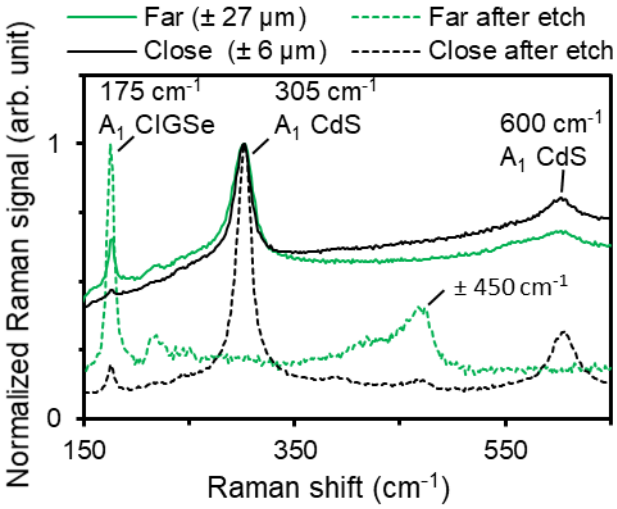

Figure 9: Normalized Raman spectra of measurements with green laser before and after HCl etching on a spot close to the edge of the defect and a spot far away from the edge of the defect. Solid lines represent measurements before etching, dashed lines represent measurements after etching. Black lines are near the edge (± 6 µm) of defect A4 and green lines are measurements on a spot far (± 27 µm) from the edge of the defect A4 of sample I-3.

Figure 9 shows normalized Raman data obtained with a green laser before and after etching. Before etching the spectra are dominated by the contribution of the CdS on both positions. The CdS contribution is accompanied by a strong reduction of the CIGSe signal and characterized by two Raman peaks around 305 and 600 cm^{-1}. An additional effect of excitation with a green laser is an enhancement of the (luminescent) background signal from the CdS. After etching the green laser Raman signal, up to 350 cm^{-1}, is almost identical to the spectrum for the red laser (not shown). These results confirm that the CdS and its Raman contribution where successfully etched away in the region far away from the defect. However, close to the edge of the defect the CdS contributions at 305 and 600 cm^{-1} are still present after etching. This means that CdS is still present close to the edge of the defect after etching, confirming the observations in the border region with the SEM-EDX measurements. Moreover, it was found that a high (A_1X / A_1 CIGSe) ratio measured with the red laser is accompanied by a dominant CdS Raman signal with the green laser after etching. Also a peak around 450 cm^{-1} was observed for all measurements with the green laser after etching. The origin of this peak is still unknown but less relevant as this peak is also present in the bulk of the sample. Additionally to the Raman peak around 450 cm^{-1}, also a reduction of the luminescent background signal was observed after etching for all measurements.

4. Discussion

Ten samples were exposed to strong reverse bias conditions. Two of these cells survived the harsh reverse bias and did not exhibit wormlike defects. In eight samples wormlike defects were formed and the efficiency of these cells was severely reduced. In these cells a large variation in the electrical conditions related to the formation of wormlike defects were measured. Two distinct propagation patterns were observed: mobile wormlike defects in samples with thin TCO and stationary wormlike defects in samples with thick TCO layers. These different propagation patterns were linked to the propagation voltage and the lateral conductivity of the TCO. Therefore, it is likely that the propagation is depending on an electric field. Furthermore, it was observed that both mobile and stationary wormlike defects consists of individual islands. This points to a propagation process based on island hopping where the hotspot or epicenter jumps from one position to another. The final important clue for the proposed propagation mechanism is the alteration of CIGSe material properties in the border region at the edge of the defect.

4.1. Compositional changes in the border region

A first indication of alterations in the CIGSe material at the edge of the wormlike defects can be found in the strong presence of CdS signals in both Raman and EDX measurements. The cadmium sulfide is expected to be etched away during the HCl treatment. A potential explanation for its presence could be the diffusion of CdS molecules into the altered CIGSe material during formation of the wormlike defect. Another clue for diffusion of CdS molecules into the absorber material is the reduction of the background signal in the Raman spectra after the HCl etching (Figure 9). The background signal in the spectrum before etching could originate from the luminescence of CdS on top of the CIGSe. After etching, the CdS on top of the CIGSe is removed and only the CdS that is diffused into the altered CIGSe material is left. The luminescent signal of CdS embedded in CIGSe is quenched and/or absorbed by the surrounding CIGSe.

Another possibility is that cadmium and sulfur diffuse separately as ions. Cadmium is known to diffuse from the buffer layer into the CIGSe absorber layer under the influence of heat. Bakker et al. [14] described defect levels indicating Cd_{Cu} antisites in the border regions of wormlike defects. Furthermore, Guthrey et al. [6] showed cadmium diffusion into the absorber in the propagation front of wormlike defects. The diffusion of cadmium into the absorber will change the electrical behavior of the solar cell in the forward region [20]. At reverse voltages the buffer layer is known to play an important role in the reverse electrical characteristic [21,22]. Considering these two facts it is likely that the pile-up of CdS is changing the electrical behavior in the border region. Lee et al.[2] reported an involvement of the buffer layer (both CdS and Zn(O,S)) in the formation of wormlike defects by partial shading on commercial CIGSe modules.

Besides changes in the buffer layer, also indications for compositional changes in the CIGSe absorber layer in the border region of the defect were found. SEM EDX measurements showed a redistribution of elements, a more detailed description of the EDX results is presented in [14]. The redistribution of indium and gallium as observed in EDX was confirmed by Raman measurement in the form of a shift in A_1 CIGSe peak position. Furthermore, a broadening of the this main Raman peak was observed in the border region. Broadening of the FWHM of the main CIGSe A_1 peak in Raman indicates a change in the crystallinity and/or in the number of lattice defects. Therefore, the elemental changes are likely accompanied by changes in the crystal lattice.

Based on the measurements, it is likely that subtle changes took place in the border region. We assume that these changes altered the electrical and chemical properties, which makes the material in the border region more vulnerable to the start of a new island.

4.2. Electric field

There are two observations besides the propagation voltage that indicate a dependency of the propagation mechanism on the electric field over the CIGSe material. Firstly, the field between Mo and TCO as the wormlike defects did not propagate into areas without Mo. This implies that an electrical connection (conductive path) between front and back contact is needed for the wormlike defect to propagate. Secondly, the difference in size and spacing of islands between the mobile and stationary wormlike defects. The stationary wormlike defects were found only on samples with thick

TCO. A thicker TCO has a higher conductivity and therefore the voltage drop over the thick TCO in case of equal current is much lower compared to TCO with normal thickness and conductivity. Because of this reduced voltage drop in samples with thicker TCO the electric field between molybdenum and TCO will be smaller for these samples in the region close to the defect.

The electric field near the defect consists of several contributions. The main contributors are displayed in Figure 10 and are: voltage drop over TCO, voltage losses in interfaces, and voltage drop inside the defect. It should be noted that negligible contributions like the Mo resistance are omitted. Since the voltage drop over the defect can not be neglected, it is shown as equal in both cases and only the ratio of losses in the TCO and the interfaces has been changed.

The voltage drop over the TCO is the only contribution to the electric field that has a dependency on the distance to the defect. An estimation of the voltage distribution (*V(r)*) over the TCO close to a point-defectcan be made using the solution of the Laplace's equation with cylindrical coordinates [23] given in equation (1). Assuming that an isolated island in a wormlike defect acts as a point defect.

$$V(r) = ln\left(\frac{r}{r_0}\right) * \frac{I * R_{sheet}}{2\pi} \tag{1}$$

In this equation r is the distance from the center of the point-defect in meter, r_0 is the radius of the point-defect in meter, I is current through the defect in Ampère and R_{sheet} is the sheet resistance in Ohm. From equation (1) it can be concluded that the size of the defect (r_0) has a large influence on the voltage gradient in the TCO: a bigger defect gives less voltage loss in the TCO. A calculation of the influence of the sheet resistance on the voltage drop over the TCO with respect to the distance of the defect is plotted in Figure 11. The sheet resistance has a linear relation to the voltage loss in equation 1.,In Figure 11 it is observed that the voltage drop is doubled when the resistance is reduced by 50 percent.

(a) Cross section of defect

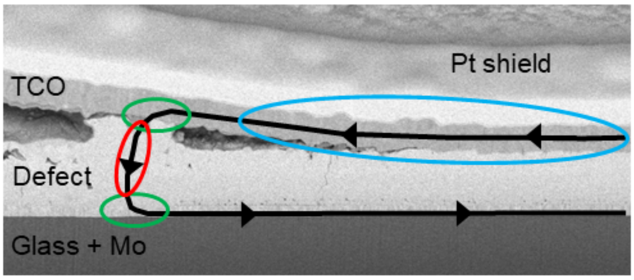

(b) Equivalent circuit

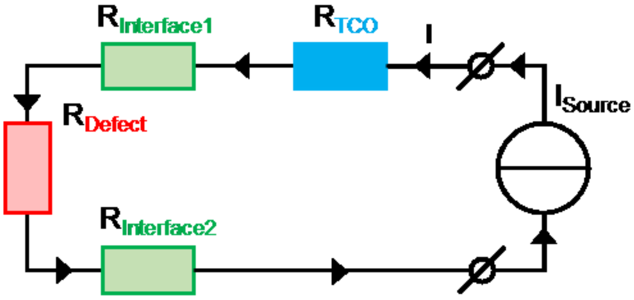

(c) Relative voltage contributions

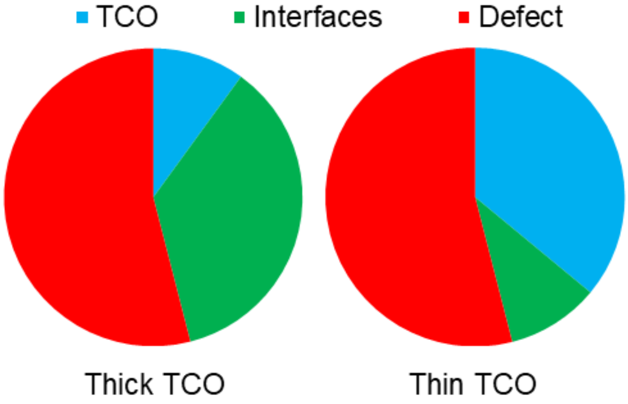

Figure 10: Visualization of voltage losses inside and near the defect. (a) SEM cross-section of a wormlike defect with indications of current flow and resistive losses. (b) Equivalent circuit showing the resistive elements indicated in (a). (c) Pie charts showing an estimation of the contribution of the different voltage losses to electric field close to the defect for cells with thick and thin TCO. The current flow in (a) and (b) is indicated with a black line and the direction of the current is given with arrows. In all figures the colors blue, green, and red represent the TCO, the nterfaces with the defect, and the defect itself, respectively.

Another major contribution to the electric field near the defect are the resistive losses at the interfaces, as shown in Figure 10. These are both ‘defect – TCO’ and ‘Mo – defect’ interfaces. It should be apparent that when the island grows and becomes more porous, the interface between the layers will change. For instance, the contact area between the defect and the TCO is reduced due to voids between the defect and the TCO when the CIGSe material expands and become more porous. An increase in contact resistance is expected for larger islands due to the relative loss in contact area and the changed (electrical) interface properties. Figure 10 (c) shows an estimation of the relative contribution to the electric field close to the defect for cells with thin and thick TCO. The voltage loss over the TCO is smaller for cells with a thick TCO layer. This can be explained by the higher conductivity of the thicker TCO layer and the larger size (r_0 in equation 1) of the islands, that were observed on samples with thick TCO. Therefore, a relation of the interface resistance with the size of the islands would explain why the islands have to expand more to get the same electric field required for propagation. The larger size of the individual islands increases the contribution of the contact resistance to reach the required voltage needed for island hopping.

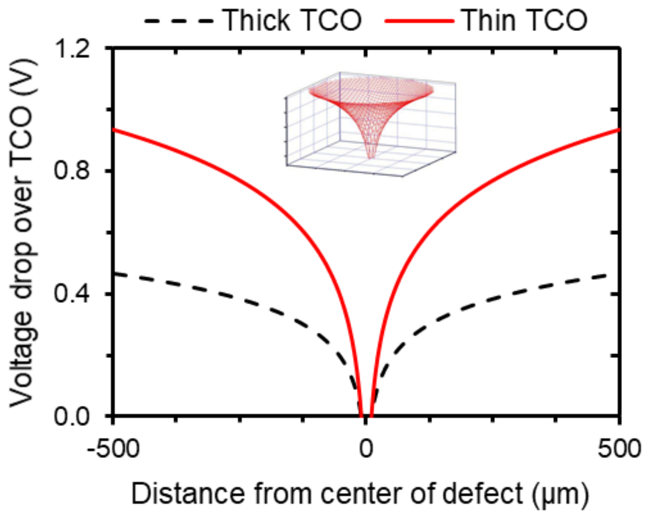

Figure 11: Voltage loss over TCO as function of distance to the center of the defect. Calculated from equation 1, assumptions made for current and the radius of defect are 100 mA and 10 µm, respectively. The center of defect is at 0, the voltage inside the defect is not plotted. Two different sheet resistances are used: thick TCO (black dashed line) 7.5 Ω and thin TCO (red line) 15 Ω. The inset shows a 3D representation of the voltage drop over the TCO, for the calculation of the sample with thin TCO. Both horizontal axis show distance and the vertical axes shows the voltage loss..

The last contribution to the electric field is the voltage loss in the defect itself. The CIGSe solar cell material has the biggest influence on this contribution as should be clear from Figure 3, that shows the dependency of the propagation voltage on the different CIGSe runs. The current flow in the defect is a combination of current flowing through the altered material at the edge of the defect and through the epicenter itself. For the propagation mechanism that is proposed in the next section, the majority of current has to flow through the epicenter. In this study a constant current was supplied during defect formation. Therefore, the current density in the edge would drop as the area of affected material at the edge grows when an islands expands. When more islands are created during the formation of a wormlike defect the current would be diluted, consequently the ohmic heating would spread out over a larger area. Because of this a propagation mechanism where the majority of the supplied current flows through the edge seems less likely. Ohmic heating at the edge of the defect would also not explain the difference in propagation mechanism between the two different TCO layers. A mechanism where after the epicenter has hopped to a new island the old island cools down and the current flow through the old island is reduced is more likely.

4.3. Proposed propagation mechanism

In order to explain the formation of wormlike defects two effects need to be explained:

- The formation and expansion of the individual islands.

- The hopping of an islands to a neighboring region.

For the proposed mechanism the formation and expansion of the individual islands is based on a chemical reaction. This reaction forms the epicenter of the moving hotspot. The temperatures inside the epicenter are high. The origin of the heat generation could be the chemical reaction itself, ohmic heating due to the high current density, or a combination of both heat sources. Furthermore, the reaction is responsible for the observed change in material properties inside the wormlike defect. The reaction requires at least:

- Fuel, which is in the form of elements or reactants that are supplied from outside the epicenter.
- Electricity, the reaction needs a minimum electric field to get started and a current to sustain itself. This is , analogue to a plasma; a plasma needs a high voltage to ignite and current to maintain its state.

Heat generation during the island formation is considerable, it is less evident if the reactions requires heat to start or to sustain itself.

The hopping mechanism involves the creation of a nucleus, allowing the formation of a new island. Nucleation occurs in the neighboring region of the epicenter. This area is referred to as the nucleation zone. Key elements needed for the nucleation that are present in the nucleation zone are:

- Poor material quality that provides plenty of seeds to start a nucleus: this is present in the modified material in the border region as evidenced by Raman spectroscopy and EDX measurements.
- Electric field: as shown with confocal microscopy, there is a strong dependence between the spacing of the islands and TCO thickness. The nucleation zone is shifted away from the epicenter in case of reduced field in cells with thick TCO.
- Heat: the nucleation is probably aided by the elevated temperature in the nucleation zone.

Figure 12 shows a schematic of the proposed propagation mechanism. The stages of propagation are:

0) Initial starting point. This could be a shunt or other local fault in CIGS material as shown by Palmiotti et al. [4].
1) Due to high current density the defect starts to heat up and becomes a local hotspot.
2) Due to heat and electricity a reaction starts. Reactants are provided by the neighboring material. The diffusion of reactants is boosted by the elevated temperature in the border region.
3) The island is expanding and the material in the border region is weakened. In the border region material changes take place due to the vacancies left by the diffused reactants. The supply of reactants gets more difficult over time since the border region starts to get depleted and reactants have to travel a greater distance. A nucleation zone with favorable conditions for propagation is formed. Favorable conditions include; heat, electric field and poor material quality.
4) A new reaction site is created from a nucleus. The supply of reactants in this new region is fresh and the gravity of the electric current flow is redirected towards the new site and the old islands starts to cool.
5) A new hotspot is formed and the reaction starts from 1.

This proposed propagation mechanism based on islands hopping explains the observed discrete islands that make up wormlike defects. Also, the dependency on electric field in the model can account for the difference between mobile and stationary wormlike defects in relation to the different TCO thicknesses on the cells.

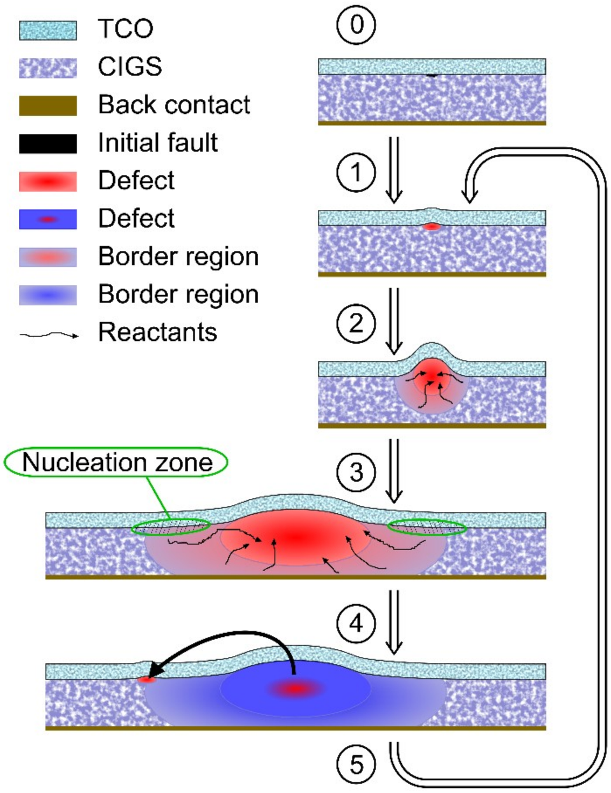

Figure 12: Schematic representation of the proposed propagation mechanism.

Conclusion

In this study a model is proposed for the propagation of reverse bias induced “wormlike” defects in CIGSe. In this model, a moving hotspot leaves a trail of damaged CIGSe material. The moving hotspot consists of a chemical reaction that hops from islands to island. Conditions required for island hopping are: poor material quality, electric field, and heat. The mobility of the hotspot can be influenced by altering the electric field near the defect by changing the TCO thickness. Thicker TCO confines the defects, the area affected is less big, and the wormlike defects do not always reach the interconnect. Power loss was less severe for wormlike defects that did not extend to the interconnection and two cells survived the harsh reverse bias exposure without the formation of wormlike defects. Hence, the negative impact on module output due to partial shading will be reduced when using cells with thicker TCO.

Acknowledgements

This work is supported by ‘Netherlands Enterprise Agency’ (RVO) and the Dutch Topteam Energy via the projects: ‘Building Integrated PhotoVoltaic Panels on Demand - in The Netherlands’ with grant number TEID215005 and ‘Performance and Electroluminescence Analysis on Reliability and Lifetime of Thin-Film Photovoltaics’ with grant number TEUE116203. Furthermore, the Early Research Program ‘Sustainability & Reliability for solar and other (opto-)electronic thin-film devices’ from TNO is acknowledged for funding.

References

[1] H. Ziar, B. Asaei, S. Farhangi, M. Korevaar, O. Isabella, M. Zeman, Quantification of Shading Tolerability for Photovoltaic Modules, IEEE J. Photovoltaics. 7 (2017) 1390–1399. doi:10.1109/JPHOTOV.2017.2711429.

[2] J.E. Lee, S. Bae, W. Oh, H. Park, S.M. Kim, D. Lee, J. Nam, C. Bin Mo, D. Kim, J. Yang, Y. Kang, H. Lee, D. Kim, Investigation of damage caused by partial shading of CuInxGa$_{(1-x)}$Se$_2$ photovoltaic modules with bypass diodes, Prog. Photovoltaics Res. Appl. 24 (2016) 1035–1043. doi:10.1002/pip.2738.

[3] P.O. Westin, U. Zimmermann, L. Stolt, M. Edoff, Reverse Bias Damage in CIGS Modules, in: 24th Eur. Photovolt. Sol. Energy Conf., 2009: pp. 2967–2970. doi:10.4229/24thEUPVSEC2009-3BV.5.34.

[4] E. Palmiotti, S. Johnston, A. Gerber, H. Guthrey, A. Rockett, L. Mansfield, T.J. Silverman, M. Al-Jassim, Identification and analysis of partial shading breakdown sites in $CuIn_xGa_{(1-x)}Se_2$ modules, Sol. Energy. 161 (2018) 1–5. doi:10.1016/j.solener.2017.12.019.

[5] S. Johnston, D. Sulas, E. Palmiotti, A. Gerber, H. Guthrey, J. Liu, L. Mansfield, T.J. Silverman, A. Rockett, M. Al-Jassim, Thin-Film Module Reverse-Bias Breakdown Sites Identified by Thermal Imaging, in: 2018 IEEE 7th World Conf. Photovolt. Energy Convers. (A Jt. Conf. 45th IEEE PVSC, 28th PVSEC 34th EU PVSEC), IEEE, 2018: pp. 1897–1901. doi:10.1109/PVSC.2018.8547766.

[6] H. Guthrey, M. Nardone, S. Johnston, J. Liu, A. Norman, J. Moseley, M. Al-Jassim, Characterization and modeling of reverse-bias breakdown in Cu(In,Ga)Se$_2$ photovoltaic devices, Prog. Photovoltaics Res. Appl. (2019) pip.3168. doi:10.1002/pip.3168.

[7] S. Johnston, E. Palmiotti, A. Gerber, H. Guthrey, L. Mansfield, T.J. Silverman, M. Al-Jassiml, A. Rockett, Identifying Reverse-Bias Breakdown Sites in CuInxGa(1-x)Se2, in: 2017 IEEE 44th Photovolt. Spec. Conf., IEEE, 2017: pp. 1400–1404. doi:10.1109/PVSC.2017.8366755.

[8] T.J. Silverman, I. Repins, Partial Shade Endurance Testing for Monolithic Photovoltaic Modules, in: 2018 IEEE 7th World Conf. Photovolt. Energy Convers. (A Jt. Conf. 45th IEEE PVSC, 28th PVSEC 34th EU PVSEC), IEEE, 2018: pp. 3932–3937. doi:10.1109/PVSC.2018.8547832.

[9] T.J. Silverman, L. Mansfield, I. Repins, S. Kurtz, Damage in Monolithic Thin-Film Photovoltaic Modules Due to Partial Shade, IEEE J. Photovoltaics. 6 (2016) 1333–1338. doi:10.1109/JPHOTOV.2016.2591330.

[10] M. Theelen, K. Beyeler, H. Steijvers, N. Barreau, Stability of CIGS solar cells under illumination with damp heat and dry heat: A comparison, Sol. Energy Mater. Sol. Cells. 166 (2017) 262–268. doi:10.1016/j.solmat.2016.12.039.

[11] M. Theelen, K. Bakker, H. Steijvers, S. Roest, P. Hielkema, N. Barreau, E. Haverkamp, In Situ Monitoring of the Accelerated Performance Degradation of Solar Cells and Modules : A Case Study for Cu(In,Ga)Se_2 Solar Cells, J. Vis. Exp. 140 (2018). doi:10.3791/55897.

[12] F. Couzinié-Devy, N. Barreau, J. Kessler, Re-investigation of preferential orientation of Cu(In,Ga)Se_2 thin films grown by the three-stage process, Prog. Photovoltaics Res. Appl. 19 (2011) 527–536. doi:10.1002/pip.1079.

[13] T. Feurer, P. Reinhard, E. Avancini, B. Bissig, J. Löckinger, P. Fuchs, R. Carron, T.P. Weiss, J. Perrenoud, S. Stutterheim, S. Buecheler, A.N. Tiwari, Progress in thin film CIGS photovoltaics - Research and development, manufacturing, and applications, Prog. Photovoltaics Res. Appl. 25 (2017) 645–667. doi:10.1002/pip.2811.

[14] K. Bakker, H. Nilsson Åhman, K. Aantjes, N. Barreau, A. Weeber, M. Theelen, Material Property Changes in Defects Caused by Reverse Bias Exposure of CIGS Solar Cells, IEEE J. Photovoltaics. (2019). doi:10.1109/JPHOTOV.2019.2940486.

[15] S. Wendlandt, L. Podlowski, Influence of Near Field Shadowing on the Performance Ratio of Thin Film Modules, in: 35th Eur. Photovolt. Sol. Energy Conf. Exhib., 2018: pp. 1230–1235. doi:10.4229/35thEUPVSEC20182018-5CV.1.35.

[16] S. Roy, P. Guha, S.N. Kundu, H. Hanzawa, S. Chaudhuri, A.K. Pal, Characterization of Cu(In,Ga)Se_2 films by Raman scattering, Mater. Chem. Phys. 73 (2002) 24–30. doi:10.1016/S0254-0584(01)00345-5.

[17] V. Izquierdo-Roca, X. Fontané, E. Saucedo, J.S. Jaime-Ferrer, J. Álvarez-García, A. Pérez-Rodríguez, V. Bermudez, J.R. Morante, Process monitoring of chalcopyrite photovoltaic technologies by Raman spectroscopy: an application to low cost electrodeposition based processes, New J. Chem. 35 (2011) 453–460. doi:10.1039/C0NJ00794C.

[18] F. Oliva, S. Kretzschmar, D. Colombara, S. Tombolato, C.M. Ruiz, A. Redinger, E. Saucedo, C. Broussillou, T.G. de Monsabert, T. Unold, P.J. Dale, V. Izquierdo-Roca, A. Pérez-Rodríguez, Optical methodology for process monitoring of chalcopyrite photovoltaic technologies: Application to low cost Cu(In,Ga)(S,Se)$_2$ electrodeposition based processes, Sol. Energy Mater. Sol. Cells. 158 (2016) 168–183. doi:10.1016/j.solmat.2015.12.036.

[19] W. Witte, R. Kniese, M. Powalla, Raman investigations of Cu(In,Ga)Se_2 thin films with various copper contents, Thin Solid Films. 517 (2008) 867–869. doi:10.1016/j.tsf.2008.07.011.

[20] S. Kijima, T. Nakada, High-Temperature Degradation Mechanism of Cu(In,Ga)Se_2-Based Thin Film Solar Cells, Appl. Phys. Express. 1 (2008) 075002. doi:10.1143/APEX.1.075002.

[21] P. Szaniawski, J. Lindahl, T. Törndahl, U. Zimmermann, M. Edoff, Light-enhanced reverse breakdown in Cu(In,Ga)Se_2 solar cells, Thin Solid Films. 535 (2013) 326–330. doi:10.1016/j.tsf.2012.09.022.

[22] S. Puttnins, S. Jander, K. Pelz, S. Heinker, F. Daume, A. Rahm, A. Braun, M. Grundmann, The Influence of Front Contact and Buffer Layer Properties on CIGSe Solar Cell Breakdown Characteristics, in: 26th Eur. Photovolt. Sol. Energy Conf. Exhib., 2011: pp. 2432–2434. doi:10.4229/26thEUPVSEC2011-3CO.4.6.

[23] P.C. Clemmow, An introduction to electromagnetic theory, University Press, Cambridge, U.K., 1973.